Chemical Engineering Journal 547 (2026) 181451

Contents lists available at ScienceDirect

Chemical Engineering Journal

journal homepage: www.elsevier.com/locate/cej

Pt nanoparticles as electron mediators in CdS/AgIn$(WO_4)_2$ nanotube heterojunctions for efficient photocatalytic hydrogen evolution

Quanmei Zhou, Jiayi Meng, Yifan Liao, Yuchen Wei, Bite Deng, Yuying Hu, Hongyan Zhao, Yakun Song, Mohan Zhang, Wei-Lin Dai *

State Key Laboratory of Porous Materials for Separation and Conversion, Shanghai Key Laboratory of Molecular Catalysis and Innovative Materials, Department of Chemistry, Fudan University, Shanghai, 200438, PR China

ARTICLE INFO

Keywords:
AgIn$(WO_4)_2$ nanotube heterostructure
Pt-mediated electron transport
Interfacial charge migration
Electron mediator
Solar-driven H_2 evolution

ABSTRACT

Solar-driven photocatalytic water splitting offers a promising route for sustainable hydrogen production. Herein, a ternary CdS/Pt/AgIn$(WO_4)_2$ photocatalyst was fabricated via hydrothermal synthesis followed by in situ photoreduction. The optimized CdS/Pt/AgIn$(WO_4)_2$ catalyst achieves a visible-light-driven hydrogen evolution rate of 6.54 mmol·g^{-1}·h^{-1}, approximately 30 and 5 times higher than those of pristine AgIn$(WO_4)_2$ nanotubes and CdS nanoparticles (CdS NPs), respectively. Combined structural characterizations and theoretical analyses confirmed the formation of a strongly coupled CdS/Pt/AgIn$(WO_4)_2$ interface. Interfacial Pt nanoparticles (Pt NPs) acted as electron mediators, facilitating directional electron transfer from CdS NPs to AgIn$(WO_4)_2$ and promoting charge separation. Density functional theory (DFT) calculations reveal that the hydrogen adsorption Gibbs free energy (ΔG_H^*) is close to the thermoneutral value, thereby reducing the thermodynamic barrier for hydrogen evolution. The synergistic effect of interfacial charge transfer and accelerated surface reaction kinetics significantly enhances the photocatalytic hydrogen evolution performance of the CdS/Pt/AgIn$(WO_4)_2$ heterostructure. This study provides an effective strategy for developing high-performance CdS-based photocatalysts for solar hydrogen production.

1. Introduction

The persistent reliance on conventional fossil resources has resulted in increasingly severe energy challenges and environmental concerns. Compared with traditional thermocatalytic and electrocatalytic technologies for hydrogen production, solar-driven semiconductor photocatalytic water splitting is regarded as an environmentally friendly and carbon-neutral approach for sustainable hydrogen generation [1–6]. Among various photocatalytic materials, tungstate-based semiconductors, such as Bi_2WO_6 [7,8], Ag_2WO_4 [9,10], and $CoWO_4$ [11,12], have attracted considerable attention owing to their favorable optoelectronic properties and chemical stability. However, their relatively positive conduction-band positions generally restrict their reduction capability. In comparison, AgIn$(WO_4)_2$ possesses suitable band structures and favorable photoelectric properties, together with a well-defined rectangular nanotube architecture, which provides abundant interfacial contact sites for coupling with other catalytic components and facilitates interfacial charge transfer [13]. These features make AgIn$(WO_4)_2$ a promising support for photocatalytic hydrogen evolution, although related studies remain relatively limited.

Meanwhile, cadmium sulfide (CdS), a typical II-VI semiconductor, has been extensively investigated for photocatalytic hydrogen evolution owing to its suitable band structure and diverse morphologies [14,15]. However, its practical application is restricted by severe photocorrosion and rapid recombination of photogenerated charge carriers, which lead to unsatisfactory photocatalytic activity and stability. To overcome these limitations, extensive efforts, including morphology regulation, elemental doping, cocatalyst decoration, and interface engineering, have been devoted to enhancing its photocatalytic performance [16–19].

Growing attention has been devoted to nanoscale structural and interfacial engineering as an effective strategy for regulating charge transfer and catalytic reaction kinetics. For example, Te/$SnSe_2$ mixed-dimensional heterostructures were constructed to regulate interfacial charge redistribution and hydrogen-evolution kinetics, while highly dispersed NiB nanoclusters deposited on g-C_3N_4 were demonstrated to

* Corresponding author.
E-mail address: wldai@fudan.edu.cn (W.-L. Dai).

https://doi.org/10.1016/j.cej.2026.181451
Received 18 July 2026; Received in revised form 27 August 2026; Accepted 31 August 2026
Available online 1 September 2026

promote charge separation and interfacial electron transfer. In addition, salt-assisted structural modulation of carbon nitride has been reported to enhance visible-light utilization and carrier dynamics. These studies highlight the significance of rational nanoscale architecture and interfacial electronic regulation in improving catalytic performance [20–22].

Recent advances have further demonstrated that rational regulation of the local coordination environment and electronic structure of active sites provides an effective strategy for enhancing catalytic performance. For instance, Zhao et al. transformed the Co-O_6 coordination configuration into coordinatively unsaturated Co-P_4 atomic sites through selective phosphidation, thereby inducing significant charge redistribution and substantially improving photocatalytic hydrogen evolution activity [23]. In addition, Liu et al. demonstrated that partial disruption of coordination bonds in mixed-ligand MOFs could induce framework amorphization and generate abundant coordinatively unsaturated metal sites, highlighting the critical role of local structural regulation in optimizing catalytic activity [24]. These recent studies underscore the importance of active-site engineering, interfacial electronic modulation, and charge redistribution in the rational design of high-performance catalysts.

Building on these advances, the construction of multicomponent photocatalytic systems with efficient interfacial charge-transfer pathways has emerged as an effective strategy for further improving photocatalytic performance [25,26]. In particular, integrating semiconductors with highly conductive electron mediators can establish intimate interfacial contact and facilitate directional migration of photogenerated carriers. Owing to their excellent electrical conductivity and favorable electron-transfer characteristics, noble-metal nanoparticles, including Pt [27,28], Au [29,30], and Ag [31,32], have been widely employed as electron mediators or cocatalysts in heterogeneous photocatalytic systems. Such mediator-assisted architectures can promote interfacial charge separation and provide efficient electron-transport channels, thereby suppressing undesirable carrier recombination and enhancing photocatalytic reaction kinetics.

In this study, a CdS/Pt/AgIn$(WO_4)_2$ ternary composite photocatalyst was successfully synthesized via a combined hydrothermal and photoreduction deposition strategy, utilizing Pt nanoparticles (NPs) as an electron-conducting bridge. Systematic optimization demonstrated that AgIn$(WO_4)_2$ decorated with 15 wt% CdS and 4 wt% Pt NPs exhibits superior visible-light-driven photocatalytic performance, achieving a remarkable H_2 evolution rate of 6.54 mmol·g^{-1}·h^{-1}. Furthermore, the integration of experimental characterizations with DFT calculations elucidates the origin of the enhanced photocatalytic performance: Pt NPs function as critical interfacial electron bridges, establishing a directional charge-transfer pathway between CdS NPs and AgIn$(WO_4)_2$. This configuration facilitates the efficient spatial migration and separation of photogenerated carriers, thereby significantly boosting the photocatalytic hydrogen evolution activity of the heterostructure.

2. Experimental

2.1. Synthesis of AgIn$(WO_4)_2$ rectangular nanotubes

AgIn$(WO_4)_2$ rectangular nanotubes were synthesized via a hydrothermal method according to a previously reported procedure [33]. Typically, 85 mg of $AgNO_3$ and 190 mg of $In(NO_3)_3$·$4.5H_2O$ were dissolved in 25 mL of deionized water under continuous magnetic stirring. The resulting solution was then added dropwise into another 25 mL of aqueous solution containing Na_2WO_4·$2H_2O$ (330 mg) and stirred vigorously until a homogeneous suspension was obtained. Subsequently, the suspension was transferred into a 100 mL of Teflon-lined stainless-steel autoclave and maintained at 180 °C for 24 h to complete the hydrothermal reaction. After naturally cooling to room temperature, the resulting precipitate was collected by centrifugation and repeatedly washed with deionized water and absolute ethanol to remove residual impurities. Finally, the product was dried at 140 °C for 4 h to obtain pure AgIn$(WO_4)_2$ powder.

2.2. Synthesis of Pt/AgIn$(WO_4)_2$ composites

In this study, Pt NPs were deposited onto AgIn$(WO_4)_2$ through a photodeposition approach [34]. Briefly, 0.09 g of the synthesized AgIn$(WO_4)_2$ powder was dispersed in 50 mL of deionized water using a 100 mL beaker and subjected to ultrasonic treatment for 30 min to obtain a homogeneous suspension. Subsequently, the suspension was transferred into a photoreactor, followed by the sequential addition of 10 mL of methanol and 0.96 mL of H_2PtCl_6·$6H_2O$ aqueous solution (10 mg/mL). The photodeposition process was conducted at 25 °C under continuous magnetic stirring. Full-spectrum irradiation was provided by a 300 W Xe lamp without a cut-off filter for 3 h. After irradiation, the solid product was collected by vacuum filtration and repeatedly washed with deionized water and absolute ethanol. Finally, the obtained grayish-black product was vacuum-dried at 80 °C overnight to afford the Pt/AgIn$(WO_4)_2$ composite containing 4 wt% Pt NPs.

Additionally, a series of AgIn$(WO_4)_2$ nanotube samples with different Pt NPs loadings were synthesized by simply adjusting the

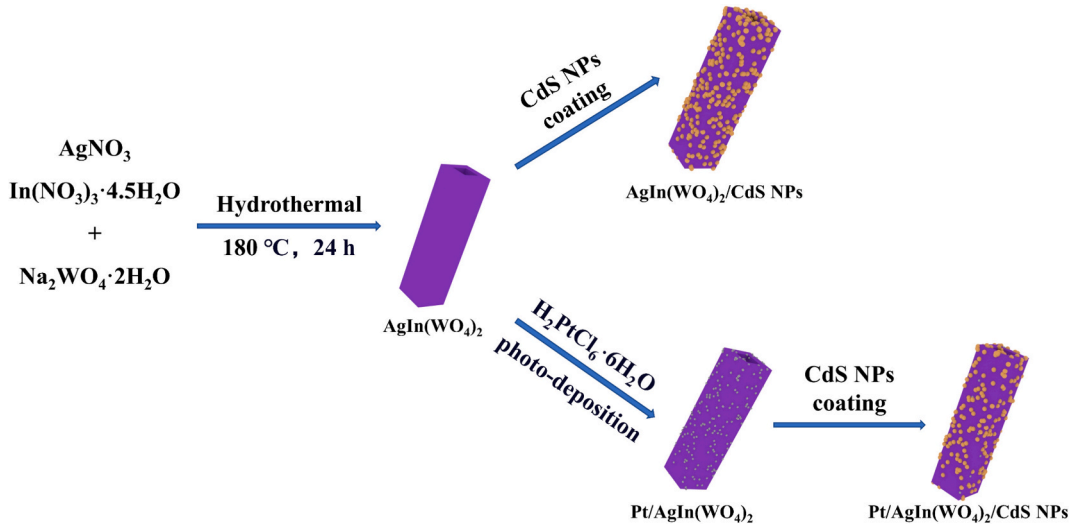

Scheme 1. Schematic illustration of the fabrication process and structural configuration of the CdS/Pt/AgIn$(WO_4)_2$ nanocomposite prepared via hydrothermal synthesis combined with photodeposition.

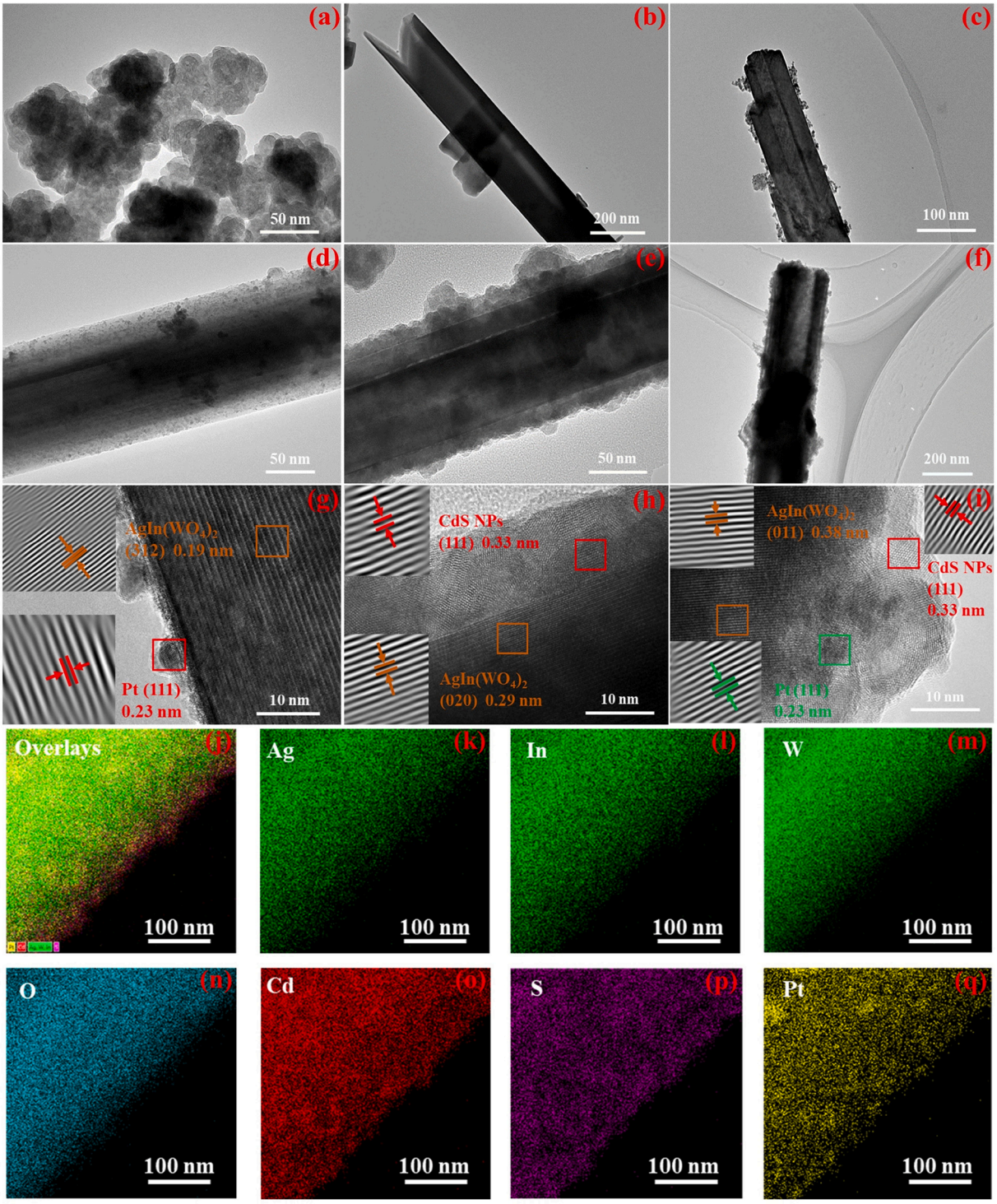

Fig. 1. TEM images of (a) CdS NPs, (b) $AgIn(WO_4)_2$, (c, d) 4% Pt/$AgIn(WO_4)_2$, (e) 15% CdS/$AgIn(WO_4)_2$, and (f) CdS/Pt/$AgIn(WO_4)_2$; (g-i) HRTEM images of Pt/$AgIn(WO_4)_2$, CdS/$AgIn(WO_4)_2$, and CdS/Pt/$AgIn(WO_4)_2$; (j-q) Corresponding EDS elemental mappings.

added volume of the $H_2PtCl_6{\cdot}6H_2O$ precursor solution. According to the Pt NPs loading amount, these composites were designated as 2% Pt/$AgIn(WO_4)_2$, 3% Pt/$AgIn(WO_4)_2$, 4% Pt/$AgIn(WO_4)_2$, and 5% Pt/$AgIn(WO_4)_2$, respectively.

2.3. Synthesis of CdS/Pt/$AgIn(WO_4)_2$ composite catalysts

Typically, 17 mg of the pre-synthesized Pt/$AgIn(WO_4)_2$ solid was uniformly dispersed in 100 mL of anhydrous ethanol under constant magnetic stirring at 80 °C for 30 min to obtain a homogeneous suspension. Subsequently, 240.0 mg of cadmium acetate dihydrate ($Cd(CH_3COO)_2{\cdot}2H_2O$) was directly added into the suspension. Meanwhile, 70 mg of thioacetamide (TAA) was dissolved in 40 mL of deionized water to form an aqueous solution. The resulting TAA solution was then gradually introduced into the above cadmium-containing suspension under vigorous stirring. The mixture was subsequently maintained at 80 °C with continuous stirring for 2 h. After the reaction, the precipitated solid was collected by centrifugation (or filtration) and repeatedly

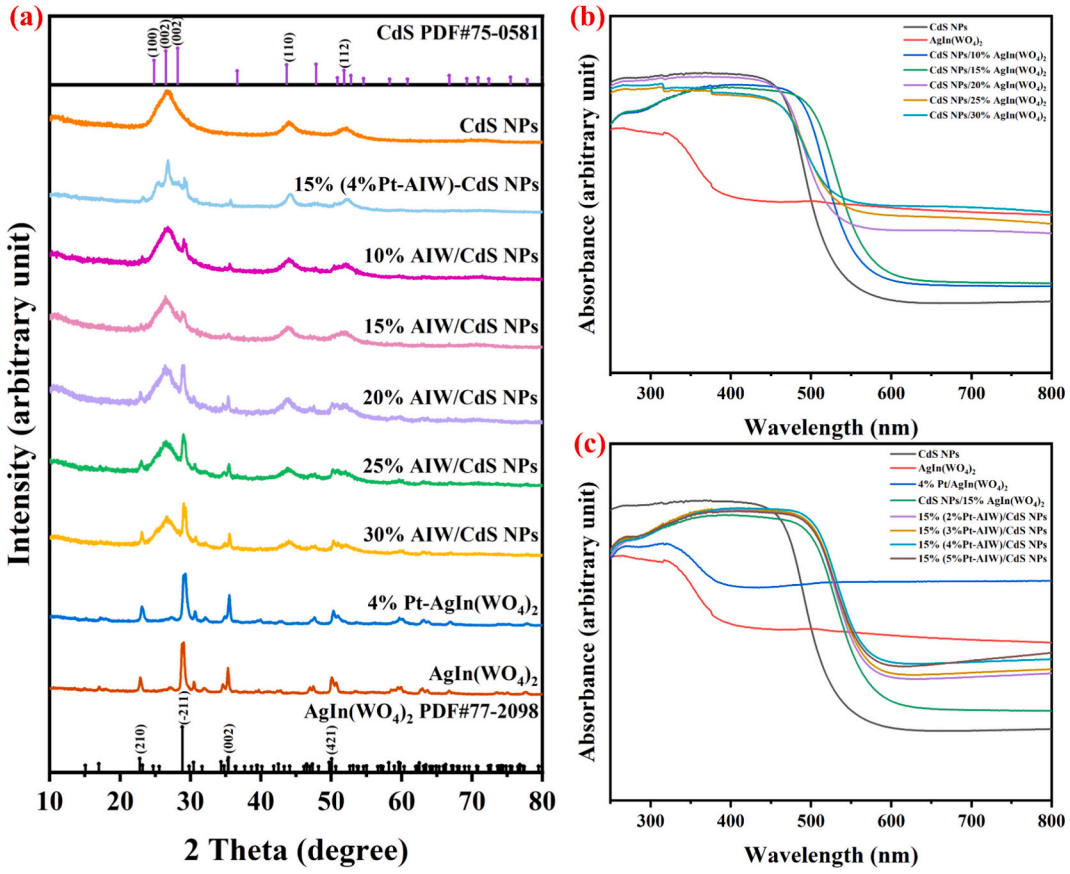

Fig. 2. (a) XRD patterns of the as-prepared samples; (b, c) UV–Vis diffuse reflectance spectra of the CdS/Pt/AgIn$(WO_4)_2$ composites.

washed with excess deionized water followed by absolute ethanol. Finally, the collected product was vacuum-dried at 60 °C for 8 h to obtain the target CdS/Pt/AgIn$(WO_4)_2$ composite catalyst.

2.4. Synthesis of CdS NPs

Following the aforementioned synthesis procedure for the CdS/Pt/AgIn$(WO_4)_2$ system, a parallel synthesis was conducted without the addition of Pt/AgIn$(WO_4)_2$ components to obtain pristine CdS NPs as a reference sample. All reaction conditions and post-treatment procedures were maintained strictly identical [35].

2.5. Characterization and computational methods

Detailed information on the experimental characterization techniques and computational methods can be found in the Supporting Information.

3. Results and discussion

3.1. Materials synthesis and characterization

Scheme 1 illustrates the synthesis route and structural evolution of the ternary CdS/Pt/AgIn$(WO_4)_2$ heterostructured photocatalyst. Initially, stable AgIn$(WO_4)_2$ rectangular nanotubes were prepared using a hydrothermal approach, serving as the supporting framework for subsequent material growth. Then, Pt NPs were deposited onto the surface of AgIn$(WO_4)_2$ nanotubes through in situ photoreduction, resulting in the formation of the Pt/AgIn$(WO_4)_2$ binary intermediate. Based on this intermediate, CdS NPs were firmly grown onto the binary interface, thereby completing the construction of the ternary composite system. For comparison, a control sample (CdS/AgIn$(WO_4)_2$) was prepared by excluding the Pt loading step. From a mechanistic perspective, the incorporated Pt NPs play a pivotal role as electron connectors. That is, they function not only as efficient electron-transfer pathways but also as bridges that ensure intimate contact between CdS NPs and AgIn$(WO_4)_2$. This robust interfacial contact not only improves structural stability but also significantly accelerates the migration of photogenerated charges, ultimately leading to a remarkable enhancement in photocatalytic hydrogen evolution performance.

To gain deeper insight into the microstructural evolution of the composites, the as-prepared samples were systematically characterized by scanning electron microscopy (SEM) and transmission electron microscopy (TEM). It was observed that pristine CdS NPs tended to aggregate into block-like structures (Fig. S1a), whereas pristine AgIn$(WO_4)_2$ exhibited a well-defined regular nanotube morphology with a smooth surface (Fig. S1b). Upon the construction of the CdS/AgIn$(WO_4)_2$ composite, the surface of the nanotubes became roughened, with a high density of CdS NPs uniformly anchored onto the tube walls (Fig. S1c). Such intimate interfacial contact increased the exposure of catalytic active sites and provided efficient pathways for the migration of photogenerated electrons.

Regarding the Pt/AgIn$(WO_4)_2$ intermediate, electron microscopy images revealed that Pt NPs were uniformly dispersed on the AgIn$(WO_4)_2$ nanotube support (Fig. S2a–c). Further structural characterization confirmed the intimate interfacial contact between Pt NPs and the nanotube support (Fig. S2d). Moreover, elemental mapping analysis demonstrated the homogeneous spatial distribution of Ag, In, W, O, and Pt throughout the entire composite, confirming the successful incorporation of all constituent elements (Fig. S2e–j).

Fig. 1 presents the microstructural characteristics of the various samples. Pure CdS NPs (8–10 nm) exhibited a strong tendency to

agglomerate, which could hinder the efficient separation of photogenerated charge carriers (Fig. 1a). In contrast, the $AgIn(WO_4)_2$ nanotubes maintained an intact tubular structure with an average diameter of approximately 40–50 nm (Fig. 1b). After in situ photodeposition, Pt NPs (approximately 10–12 nm) were successfully deposited onto the nanotube surfaces. Although slight agglomeration was observed in some regions with higher Pt loading, the overall distribution of Pt NPs remained highly uniform (Fig. 1c–d). For the control sample without Pt NPs, CdS NPs were also uniformly distributed on the surface of the nanotubes (Fig. 1e).

In the final ternary CdS/Pt/$AgIn(WO_4)_2$ system (Fig. 1f), the tubular framework of $AgIn(WO_4)_2$ nanotubes remained well preserved. The Pt NPs played a critical role as connectors in this architecture: some CdS NPs were directly attached to the nanotube walls, whereas others were grown with Pt NPs serving as nucleation sites, resulting in a dual-attachment configuration. Notably, the size of CdS NPs in the ternary system (8–10 nm) remained comparable to that of the previous samples, indicating that the in situ growth process did not significantly affect the particle morphology. Furthermore, based on the contrast variation in the electron microscopy images, it was clearly observed that the outer CdS NPs surrounded the internal Pt NPs, thereby achieving intimate interfacial integration.

HRTEM analysis (Fig. 1g–h) further confirms the formation of strong interfacial coupling among the components. The lattice fringes with spacings of 0.23 and 0.19 nm can be assigned to the (111) plane of Pt [36,37] and the (312) plane of $AgIn(WO_4)_2$, respectively, while the spacings of 0.33 and 0.29 nm correspond to the (111) plane of CdS [38,39] and the (020) plane of $AgIn(WO_4)_2$, respectively. At the heterointerface (Fig. 1i), Pt NPs act as interfacial bridges connecting CdS NPs with the $AgIn(WO_4)_2$ nanotube framework, thereby establishing a continuous electron-transport pathway responsible for the enhanced catalytic performance. EDS elemental mapping (Fig. 1j–q) and quantitative analysis (Fig. S3a–b) reveal the homogeneous distribution of Ag, In, W, O, Cd, S, and Pt without obvious elemental segregation, confirming the successful construction of the multicomponent heterostructure.

Furthermore, to evaluate the practical durability of the composite material under realistic operating conditions, comprehensive post-reaction characterizations were performed on the catalyst after multiple photocatalytic cycling tests (Figs. S4 and S5). Electron microscopy observations (Fig. S4a–c) demonstrate that, even after repeated use, the material maintains an intact one-dimensional tubular structure without obvious morphological collapse or particle aggregation. Meanwhile, distinct lattice fringes can still be clearly observed in the HRTEM images (Fig. S4d), indicating the excellent preservation of the crystal lattice structure during the photocatalytic process. Corresponding elemental mapping (Fig. S4e–l) and EDS analysis (Fig. S5a–b) further reveal that the spatial distribution and relative contents of the constituent elements in the recycled material remain nearly unchanged compared with the fresh samples. Overall, these comprehensive post-reaction characterizations confirm that the CdS/Pt/$AgIn(WO_4)_2$ composite exhibits excellent structural stability and robust cycling durability in terms of morphological retention, interfacial integrity, and chemical composition.

X-ray diffraction (XRD) analysis was conducted to investigate the crystal structures of the as-prepared composites (Fig. 2a). The diffraction pattern of pristine $AgIn(WO_4)_2$ is in excellent agreement with the standard diffraction card, indicating its high crystallinity. Pure-phase CdS NPs exhibit characteristic diffraction peaks at $2\theta \approx 26.5^\circ$, 44.0°, and 52.0°, which can be indexed to the (002), (110), and (112) crystal planes of hexagonal CdS [40,41], respectively. No additional impurity peaks are detected, confirming the high phase purity of the synthesized samples. In the binary Pt/$AgIn(WO_4)_2$ system, no obvious diffraction peaks corresponding to Pt are observed, which may be attributed to the ultrasmall size, low loading amount, and peak broadening effect of Pt NPs. In contrast, the CdS/$AgIn(WO_4)_2$ composite displays the characteristic diffraction peaks of both components, with the diffraction intensities of $AgIn(WO_4)_2$ increasing with its increasing mass fraction. This confirms the successful in situ growth of CdS NPs while maintaining the structural stability of the $AgIn(WO_4)_2$ substrate. For the ternary CdS/Pt/$AgIn(WO_4)_2$ system, Pt-related diffraction signals remain undetected, likely due to the ultrasmall size and effective encapsulation of Pt NPs by the outer CdS layer. The main diffraction peaks of $AgIn(WO_4)_2$ show no obvious shift compared with those of the pristine substrate, suggesting that heterogeneous nucleation does not significantly alter its intrinsic crystal lattice. Meanwhile, the stable CdS diffraction peak at $2\theta \approx 26.5^\circ$ further confirms its successful incorporation into the composite structure. Furthermore, the post-cycling XRD patterns (Fig. S6) exhibit no peak shifts or newly generated secondary phases, demonstrating the excellent structural stability of the composite during the photocatalytic reaction.

Raman spectroscopy (Fig. S7) further provides insights into the interfacial interactions among different components [42,43]. Pure CdS NPs exhibit a pronounced Raman band at approximately 300 cm^{-1}. Although this characteristic band is retained in the ternary composite, its intensity is significantly reduced, indicating enhanced electronic coupling and stronger interfacial interactions between CdS NPs and $AgIn(WO_4)_2$. These results are consistent with the XRD analysis and further confirm the formation of strongly coupled heterointerfaces, which facilitate efficient charge separation and rapid carrier transport.

In the photocatalytic H_2 evolution, optical absorption plays a fundamental role in determining solar energy conversion efficiency. To elucidate the origin of the enhanced photocatalytic performance, UV–Vis diffuse reflectance spectroscopy (UV–Vis DRS) was employed to investigate the optical absorption characteristics of the as-prepared samples (Fig. 2b–c) [44,45]. Pristine $AgIn(WO_4)_2$ exhibits strong UV absorption with an absorption edge at approximately 315 nm but limited visible-light response, whereas CdS NPs display a broad visible-light absorption region with an absorption edge of 500–520 nm. The CdS/$AgIn(WO_4)_2$ composite demonstrates enhanced visible-light harvesting accompanied by a slight red shift of the absorption edge, suggesting improved interfacial coupling and extended utilization of solar light.

Incorporating Pt NPs into the ternary system further optimizes the optical properties, leading to enhanced long-wavelength absorption (600–800 nm) with increasing Pt NPs loading. This indicates that Pt NPs contribute not only to the improvement of spectral response but also to the subsequent efficient separation and directional migration of photogenerated charges. Overall, these results demonstrate that the CdS/Pt/$AgIn(WO_4)_2$ heterojunction achieves enhanced broadband light absorption, thereby improving light harvesting capability and providing favorable conditions for suppressing charge recombination and promoting efficient photocatalytic hydrogen production.

N_2 adsorption-desorption measurements were conducted to investigate the pore structures of the as-prepared photocatalysts [46,47]. All samples exhibit typical type IV adsorption-desorption isotherms with well-defined hysteresis loops (Fig. S8a-d), indicating the presence of mesoporous structures. The Brunauer-Emmett-Teller (BET) specific surface areas calculated from Fig. S8e are 13.5, 20.5, 17.2, and 18.6 $m^2 g^{-1}$ for pristine $AgIn(WO_4)_2$, CdS NPs, the binary composite, and the ternary composite, respectively. Compared with the pristine substrate, the increased specific surface areas of the composites provide more exposed active sites and alleviate mass-transfer limitations, thereby offering a favorable structural basis for efficient photocatalytic H_2 evolution.

Furthermore, the average pore diameters of $AgIn(WO_4)_2$, CdS NPs, and the corresponding composites are 11.8, 14.1, 16.2, and 15.2 nm, respectively (Fig. S9). The coupled systems exhibit more developed porous networks, which can facilitate reactant diffusion at the solid-liquid interface. Notably, the slight decrease in pore diameter observed for the ternary composite may be attributed to the partial occupation of intrinsic pore channels by deposited Pt NPs. Overall, the

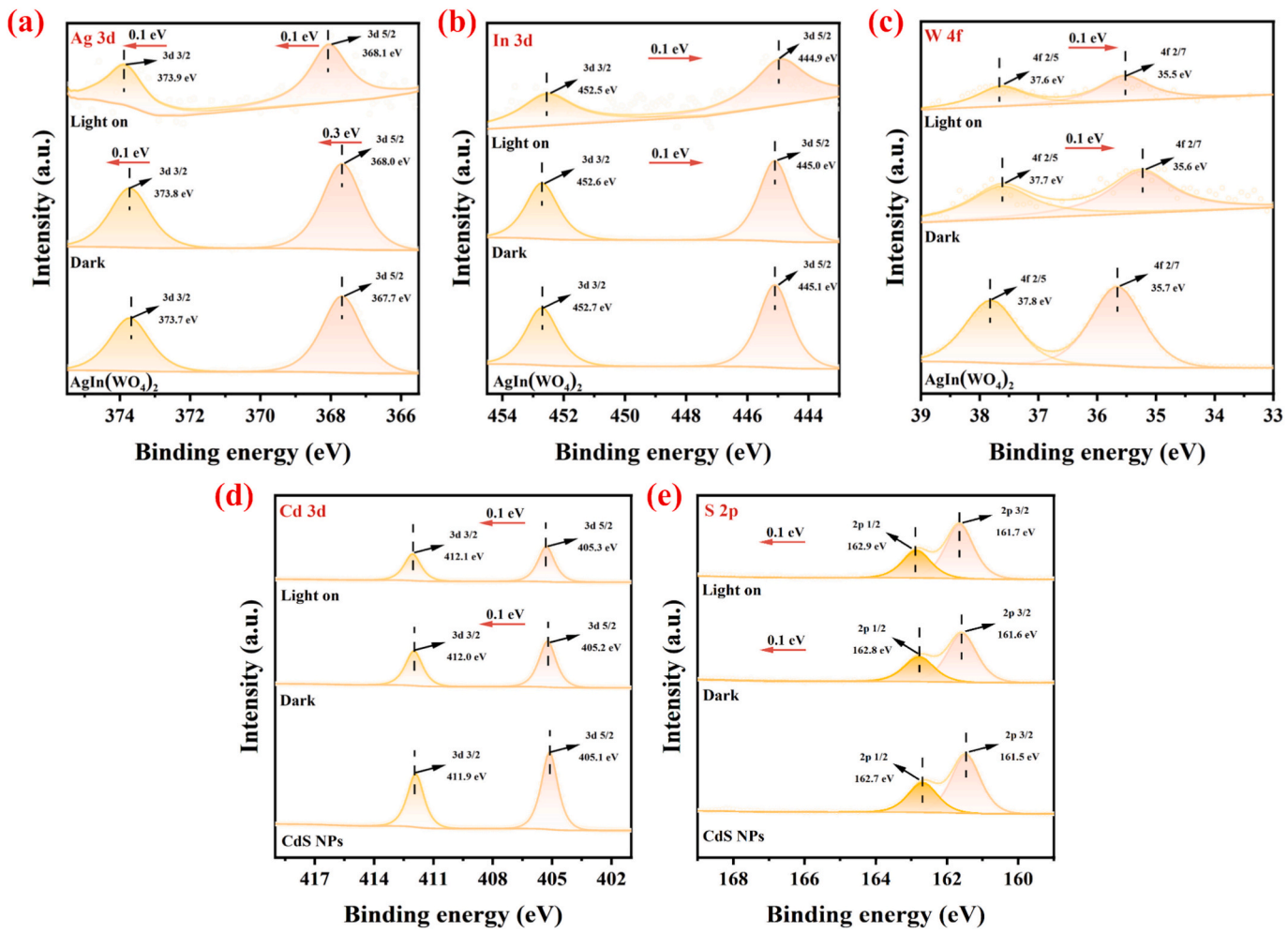

Fig. 3. XPS spectra of $AgIn(WO_4)_2$, CdS NPs, CdS/$AgIn(WO_4)_2$ and CdS/Pt/$AgIn(WO_4)_2$: (a) Ag 3d, (b) In 3d, (c) W 4f, (d) Cd 3d, and (e) S 2p.

optimized textural properties of the CdS/Pt/$AgIn(WO_4)_2$ composite provide a favorable microenvironment for enhanced photocatalytic performance (detailed parameters are summarized in Table S1).

To precisely characterize the elemental composition, surface chemical states, and bonding environments of the CdS/Pt/$AgIn(WO_4)_2$ photocatalytic composites, X-ray photoelectron spectroscopy (XPS) analysis was performed [48,49]. Fig. S10 presents the survey-scan XPS spectra of the as-prepared catalysts, in which the characteristic signals of the constituent elements are clearly identified. These elemental signals are consistently observed in pristine CdS NPs, the $AgIn(WO_4)_2$ support, as well as the corresponding binary and ternary composite samples. This observation confirms the successful incorporation and distribution of different components within the composites, which is consistent with the results obtained from energy-dispersive spectroscopy (EDS) and XRD analyses. The agreement among multiple characterization techniques further supports the successful construction of the target catalytic system and provides a reliable basis for subsequent investigation of interfacial interactions.

Fig. S11 presents the high-resolution C 1s XPS spectra of $AgIn(WO_4)_2$, CdS NPs, and the corresponding composite samples. All binding energies were calibrated using the adventitious C 1s peak as a reference. The C 1s spectra exhibit similar peak positions with only negligible variations after composite formation and light irradiation, indicating the reliability of the energy calibration process.

Fig. 3 presents the high-resolution XPS spectra of the Ag 3d, In 3d, W 4f, Cd 3d, and S 2p regions of the catalysts. The Ag 3d peaks located at approximately 367.7 and 373.7 eV are assigned to the Ag $3d_{5/2}$ and Ag $3d_{3/2}$ orbitals, respectively. After composite formation and light irradiation, these peaks exhibit a slight positive shift toward higher binding energies, suggesting that the local electronic environment of Ag becomes relatively electron-rich and participates in the interfacial charge redistribution process (Silver is a unique element where electron enrichment leads to an increase in the Ag 3d binding energy.). For the In 3d spectra, the signals centered at ~445.1 eV ($3d_{5/2}$) and ~452.7 eV ($3d_{3/2}$) shift noticeably toward lower binding energies after irradiation, indicating electron accumulation around the In atoms. Similarly, the W 4f peaks located at 35.7 eV for W $4f_{7/2}$ and 37.8 eV for W $4f_{5/2}$ shift toward lower binding energies, further confirming electron enrichment around W atoms. Collectively, these results demonstrate that $AgIn(WO_4)_2$ acts as an electron acceptor, effectively capturing photogenerated electrons under illumination.

Conversely, the characteristic Cd 3d signals centered at ~405.1 eV for Cd $3d_{5/2}$ and ~411.9 eV for Cd $3d_{3/2}$ shift toward higher binding energies after irradiation. Meanwhile, the S 2p peaks located at 161.5 and 162.7 eV, corresponding to S $2p_{3/2}$ and S $2p_{1/2}$, respectively, exhibit similar positive shifts in binding energy. These positive shifts indicate electron depletion around both Cd and S species, suggesting the migration of electrons away from CdS NPs under light irradiation.

In summary, the light-induced XPS binding-energy shifts provide experimental support for the directional electron migration from CdS NPs to $AgIn(WO_4)_2$ under illumination. Specifically, the positive shifts of the Cd 3d and S 2p peaks indicate electron depletion in CdS NPs, whereas the negative shifts of the In 3d and W 4f peaks suggest electron accumulation in $AgIn(WO_4)_2$. These opposite binding-energy shifts

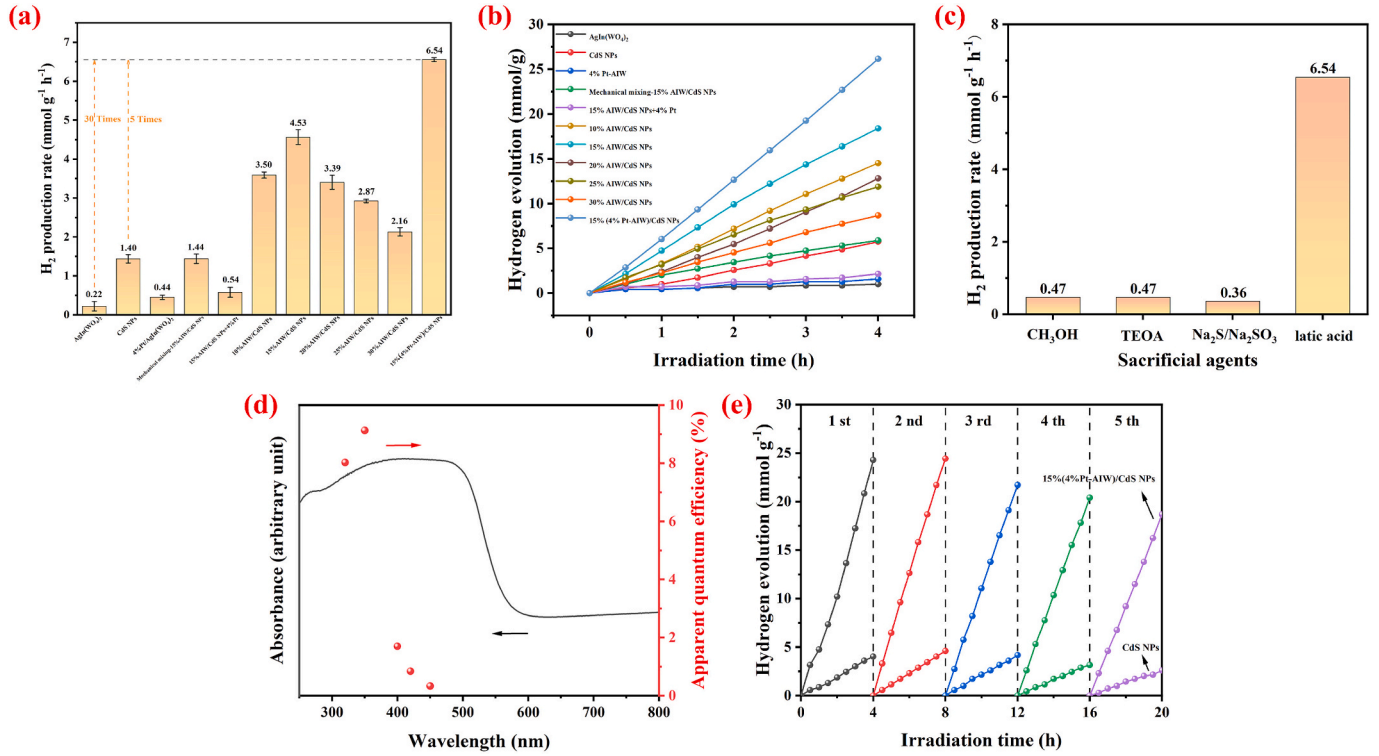

Fig. 4. (a, b) Photocatalytic hydrogen evolution activities of the CdS/Pt/$AgIn(WO_4)_2$ system; (c) H_2 evolution performance of CdS/Pt/$AgIn(WO_4)_2$ different sacrificial reagents; (d) Apparent quantum efficiency of CdS/Pt/$AgIn(WO_4)_2$; (e) Recycling photocatalytic H_2 evolution performance of CdS/Pt/$AgIn(WO_4)_2$.

further verify the proposed interfacial electron-transfer direction, which is further supported by the subsequent band-structure and work-function analyses. Such directional charge migration promotes the spatial separation and interfacial transport of photogenerated carriers, thereby contributing to the enhanced photocatalytic performance of the composite system.

3.2. *Photocatalytic performance evaluation of CdS/Pt/AgIn(WO4)2*

To evaluate the photocatalytic activity of the CdS/Pt/$AgIn(WO_4)_2$ composites, hydrogen evolution reactions were conducted under visible-light irradiation ($\lambda > 420$ nm). Fig. 4a compares the photocatalytic H_2 evolution performances of different samples. Pristine $AgIn(WO_4)_2$ and CdS NPs exhibit relatively low hydrogen evolution rates (HERs) of 0.22 and 1.40 mmol·g^{-1}·h^{-1}, respectively. In contrast, the optimized 15% (4% Pt/$AgIn(WO_4)_2$)/CdS NPs composite achieves an outstanding HER rate of 6.54 mmol·g^{-1}·h^{-1}, exhibiting superior H_2 evolution performance compared with the control samples and representative photocatalysts reported in the literature (Fig. S12 and Table S2). This remarkable enhancement can be attributed to the constructed heterojunction architecture, which facilitates efficient charge separation and suppresses the recombination of photogenerated carriers.

To further optimize the Pt NPs loading, the photocatalytic H_2 evolution performances of 15% (Pt/$AgIn(WO_4)_2$)/CdS NPs composites with different Pt NPs contents were systematically evaluated (Fig. S13), and 4 wt% Pt NPs was determined to be the optimal loading. The contents of CdS NPs and Pt NPs play crucial roles in regulating the photocatalytic H_2 evolution performance. At a relatively low CdS NPs content, insufficient visible-light absorption and limited photogenerated carrier generation restrict the photocatalytic activity. Increasing the CdS NPs content enhances visible-light harvesting and promotes interfacial charge separation and migration. However, excessive CdS NPs loading may induce particle aggregation and partially cover the catalytic surface, thereby weakening effective interfacial contact and accelerating charge recombination. Similarly, insufficient Pt NPs loading cannot provide sufficient electron-transfer pathways and catalytic sites for efficient interfacial charge migration, whereas excessive Pt NPs loading may result in particle aggregation and partial shielding of the photocatalyst surface, reducing light utilization and the availability of active sites. Therefore, appropriate CdS NPs and Pt NPs contents are essential for balancing light harvesting, interfacial charge transfer, and surface reaction kinetics, ultimately achieving optimized photocatalytic H_2 evolution performance.

Table 1
Detailed data used for AQE calculation of CdS/Pt/$AgIn(WO_4)_2$.

Wavelength (nm)	320	350	400	420	450
AQE (%)	0.33	0.73	1.07	1.20	1.33

Furthermore, ICP-OES analysis was conducted to verify the chemical composition of the optimal samples (Tables S3 and S4). The results demonstrate that the experimentally determined molar ratios of the constituent elements are consistent with the theoretical feeding ratios, confirming the successful incorporation of Pt NPs and CdS NPs into the $AgIn(WO_4)_2$ framework.

Fig. 4b shows that the cumulative H_2 yield increases linearly with irradiation time, and the optimized composite maintains the highest hydrogen evolution rate, indicating its continuous contribution to photogenerated electron utilization during the reaction. Comparative experiments using different sacrificial agents (Fig. 4c) reveal that lactic acid delivers the highest HER rate (6.54 mmol·g^{-1}·h^{-1}), outperforming CH_3OH, TEOA, and Na_2S/Na_2SO_3, and thus acts as an efficient electron donor for the photocatalytic hydrogen evolution reaction. Furthermore, Fig. 4d and Table 1 demonstrate that the composite possesses a broad visible-light response, achieving a maximum apparent quantum efficiency (AQE) of 9.13% in the wavelength range of 400–450 nm.

Regarding recyclability, pristine CdS NPs suffer from severe photocorrosion and continuous activity decay during repeated cycling tests, whereas the CdS/Pt/$AgIn(WO_4)_2$ composite maintains stable

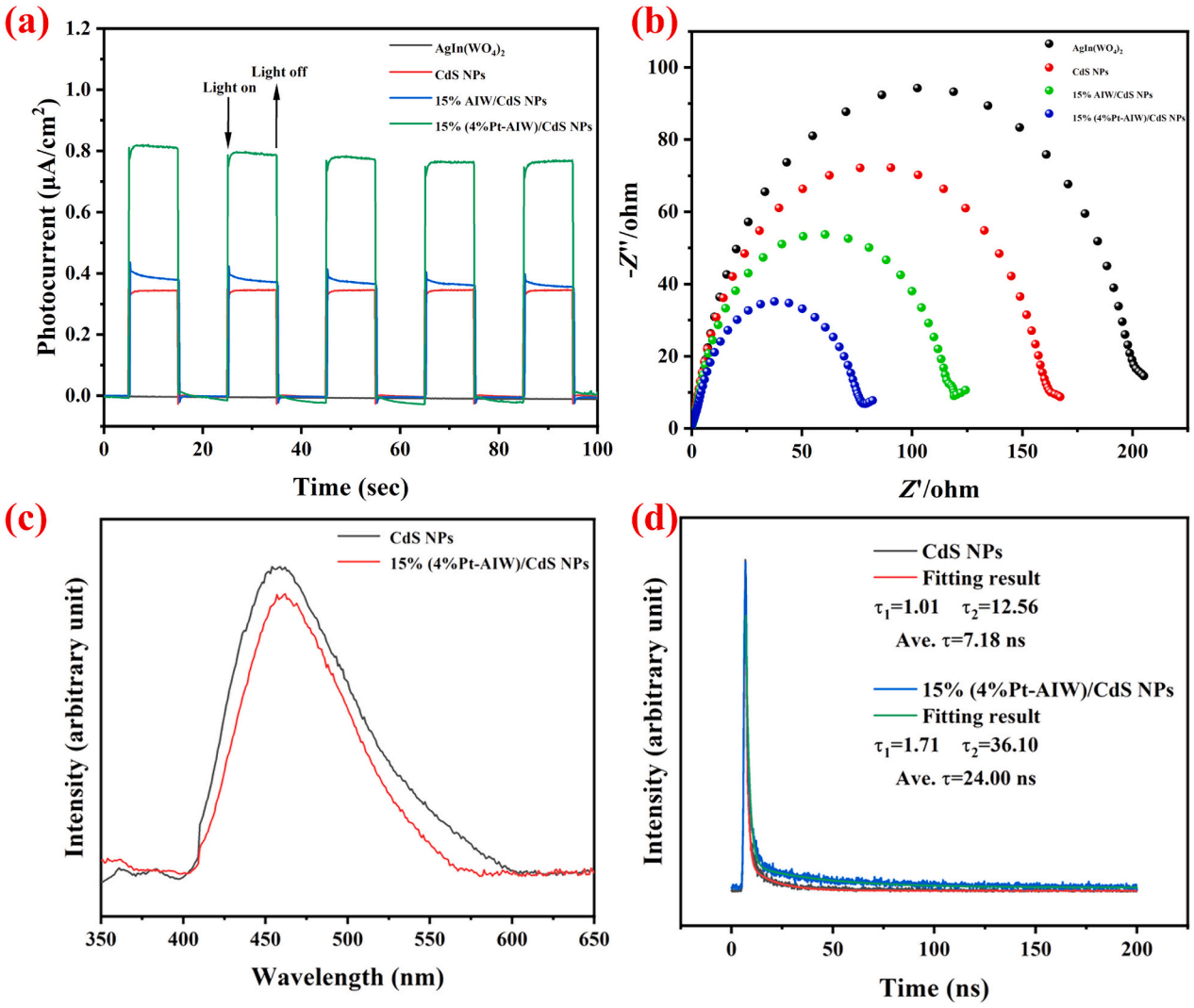

Fig. 5. (a) Transient photocurrent response; (b) EIS Nyquist plots; (c) Photoluminescence spectra; and (d) Time-resolved photoluminescence spectra of CdS/Pt/AgIn $(WO_4)_2$ system.

photocatalytic performance with negligible activity loss after five cycles (Fig. 4e). This comparison demonstrates that the introduction of Pt NPs and $AgIn(WO_4)_2$ effectively suppresses the photocorrosion of CdS NPs and improves the structural stability of the composite. In summary, the CdS/Pt/$AgIn(WO_4)_2$ composite benefits from its well-designed heterojunction architecture and the cocatalytic role of Pt NPs, enabling efficient interfacial charge transfer. Electrons preferentially accumulate on $AgIn(WO_4)_2$, while holes remain on CdS NPs, thereby simultaneously enhancing photocatalytic activity and long-term stability.

3.3. Charge-carrier separation and migration efficiency

To elucidate the charge-separation and transport behaviors in the CdS/Pt/$AgIn(WO_4)_2$ composite system, photocurrent and optical response measurements were performed. As shown in Fig. 5a, the transient photocurrent (TPC) [50] response of the composite is significantly higher than those of pristine CdS NPs and $AgIn(WO_4)_2$ nanotube. The composite exhibits rapid and reproducible photocurrent switching behavior under light irradiation, demonstrating that the heterojunction architecture effectively promotes the spatial separation and migration of photogenerated carriers. The EIS Nyquist plots [51] in Fig. 5b reveal that the composite possesses the smallest arc radius among the investigated samples, indicating reduced interfacial charge-transfer resistance and more efficient electron transport, which is favorable for the photocatalytic reaction. Furthermore, the photoluminescence (PL) spectra [52] (Fig. 5c) show that the composite exhibits weaker emission intensity than pristine CdS NPs, suggesting suppressed radiative recombination of photogenerated electron-hole pairs. Time-resolved photoluminescence (TRPL) measurements [53] (Fig. 5d) further demonstrate that the average fluorescence lifetime increases from 7.18 ns for pristine CdS NPs to 24.0 ns for the 15% (4% Pt/$AgIn(WO_4)_2$)/CdS NPs composite. The reduced steady-state PL emission intensity and prolonged TRPL decay lifetime together indicate inhibited carrier recombination and prolonged survival of photogenerated charge carriers in the composite.

Combined with the enhanced photocurrent response and decreased interfacial charge-transfer resistance, these results confirm the improved charge separation and transport capability of the CdS/Pt/$AgIn(WO_4)_2$ heterostructure. These findings highlight the important role of the heterojunction interface and Pt NPs in facilitating efficient charge migration and separation. Overall, the CdS/Pt/$AgIn(WO_4)_2$ composite achieves enhanced charge separation and interfacial transport while suppressing undesirable carrier recombination, thereby contributing to its superior photocatalytic H_2 evolution performance.

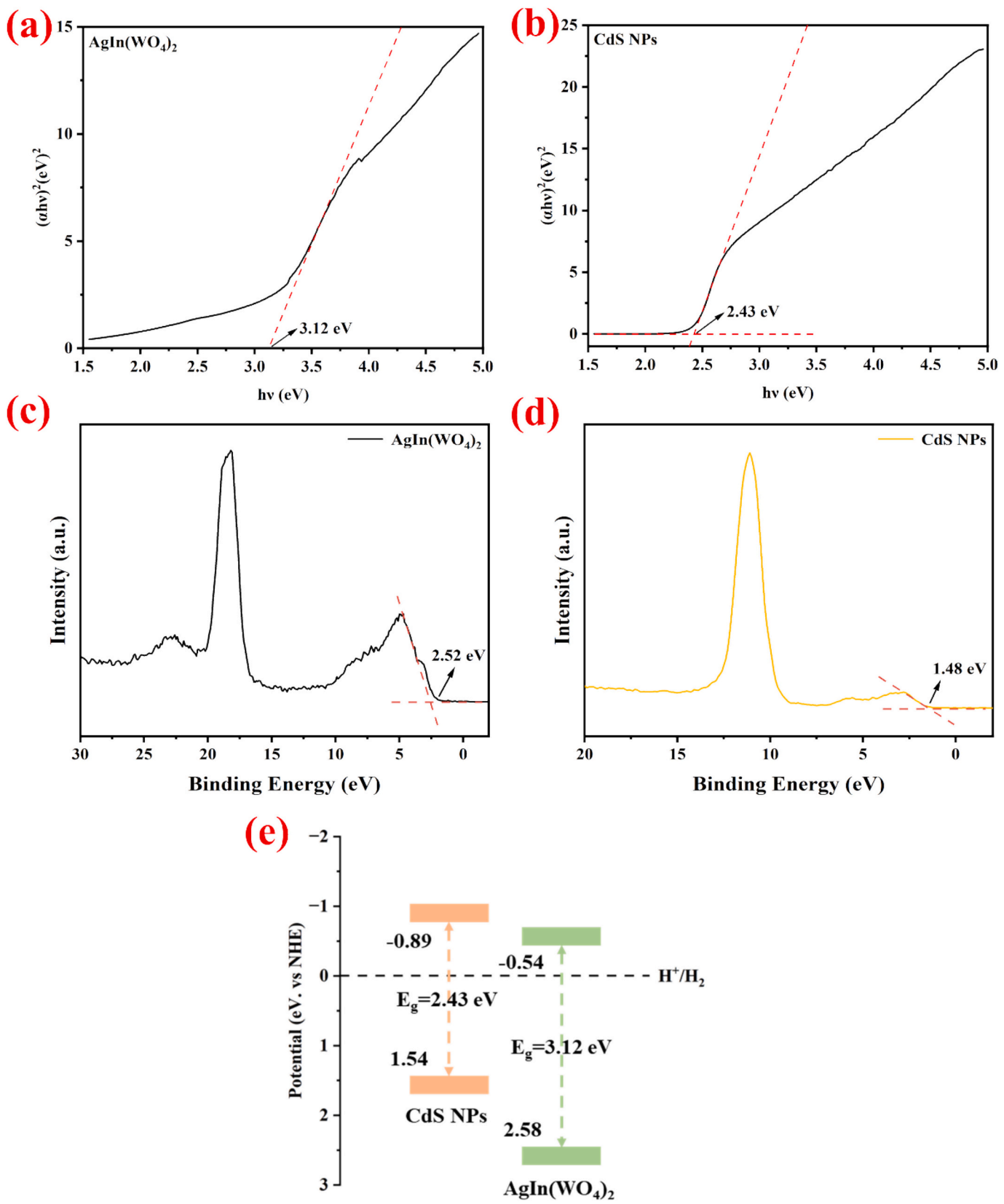

Fig. 6. (a, b) Kubelka-Munk conversion plots of the CdS/Pt/$AgIn(WO_4)_2$ system; (c, d) XPS valence band spectra of the prepared samples; (e) Band structure diagram of the composite.

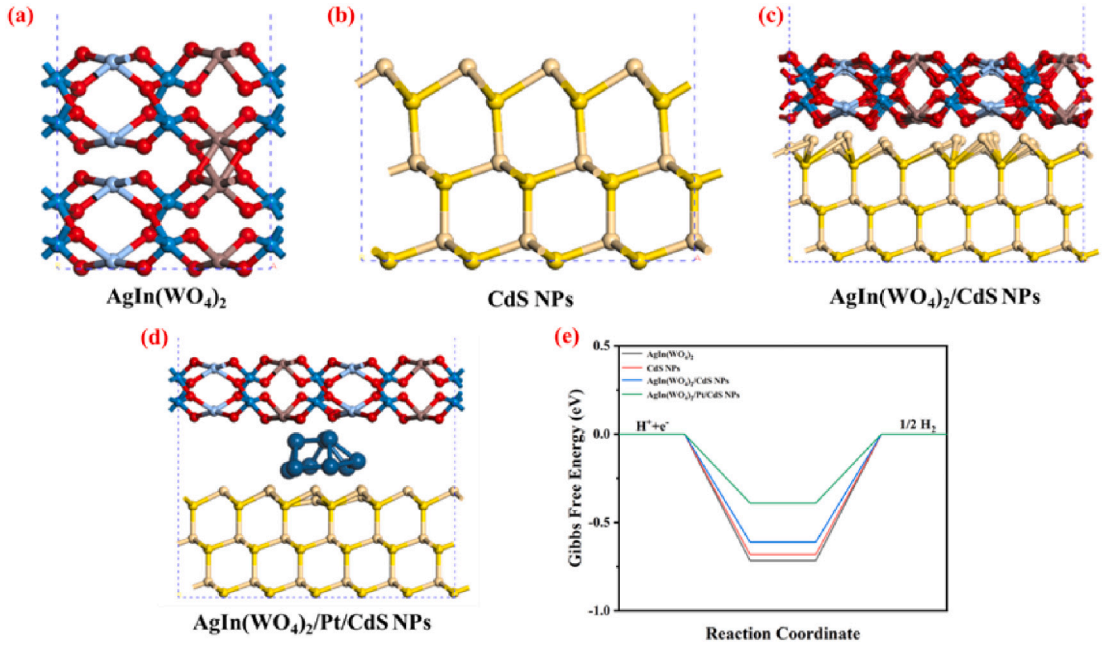

Fig. 7. (a–d) Schematic configurations of H* adsorption sites on different catalysts; (e) Gibbs free energy diagram for the hydrogen evolution reaction over the catalysts.

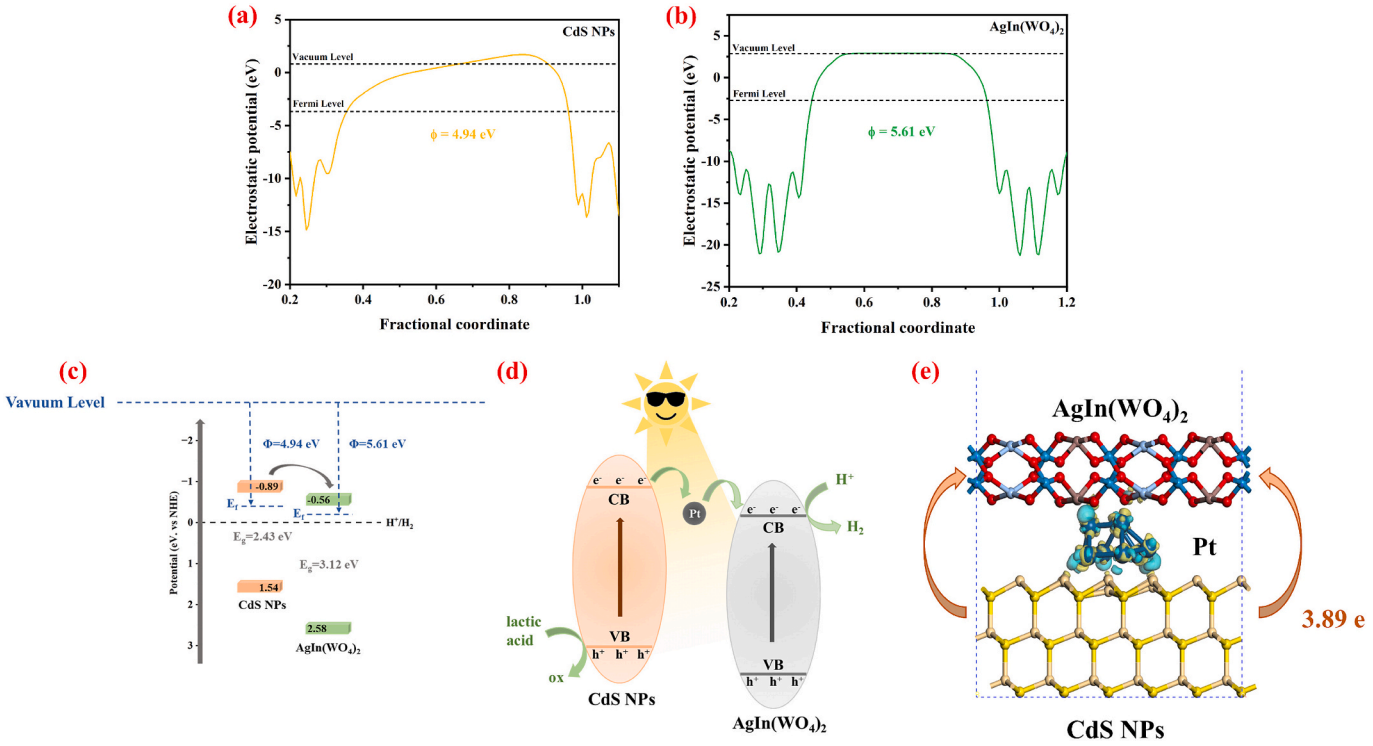

Fig. 8. Calculated electrostatic potentials of (a) CdS NPs, and (b) $AgIn(WO_4)_2$; (c) Schematic representation of the band alignment between CdS NPs and AgIn $(WO_4)_2$; (d) Schematic illustration of the type-II charge separation and migration pathway in the CdS/Pt/$AgIn(WO_4)_2$ system; (e) Electron-transfer process in the CdS/Pt/$AgIn(WO_4)_2$ system.

3.4. Theoretical analysis and charge-transfer mechanism

According to the UV–Vis DRS results, the band gaps were determined using the Kubelka-Munk function [54], as shown in Fig. 6a–b. The optical band gaps (E_g) of $AgIn(WO_4)_2$ and CdS NPs were estimated to be approximately 3.12 and 2.43 eV, respectively. Combined with the valence-band XPS spectra presented in Fig. 6c–d, the valence band (VB) positions of $AgIn(WO_4)_2$ and CdS NPs were determined to be 2.52 and 1.48 eV, respectively. The VB potentials relative to the normal hydrogen electrode (NHE) were further converted according to the following equation: $E_{VB,\ NHE} = \Phi + E_{VB,\ XPS}$ - 4.44 (where $\Phi = 4.5$ eV represents the spectrometer work function), giving values of 2.58 and 1.54 eV for AgIn $(WO_4)_2$ and CdS NPs, respectively. Furthermore, based on the equation $E_g = E_{VB} - E_{CB}$, the conduction band (CB) edge potentials of $AgIn(WO_4)_2$

and CdS NPs were calculated to be −0.54 eV and −0.89 eV, respectively. Based on these calculated parameters, the band alignment diagram shown in Fig. 6e was constructed. The obtained band configuration clearly indicates the formation of a type-II heterojunction [55].

DFT calculations were conducted to elucidate the electron-transfer pathways and photocatalytic reaction kinetics within the catalytic system. As shown in Fig. 7a–e, the Gibbs free energy of hydrogen adsorption (ΔG_H^*) was calculated by constructing hydrogen adsorption models. As a critical descriptor for evaluating photocatalytic hydrogen evolution activity, a ΔG_H^* value approaching zero represents an optimized hydrogen adsorption strength and favorable catalytic kinetics. Compared with pristine $AgIn(WO_4)_2$, CdS NPs, and the CdS/$AgIn(WO_4)_2$ binary composite, the CdS/Pt/$AgIn(WO_4)_2$ ternary composite exhibits a ΔG_H^* value closest to the ideal thermoneutral value of zero, demonstrating its favorable thermodynamic characteristics for surface hydrogen evolution. Furthermore, these results reveal that Pt NPs act as efficient electron-transfer mediators within the heterostructure, facilitating electron migration from CdS NPs to $AgIn(WO_4)_2$ and lowering the reaction energy barrier, thereby improving the overall photocatalytic hydrogen evolution performance [56,57].

To further elucidate the charge-transfer behavior and heterojunction-induced mechanisms in the CdS/Pt/$AgIn(WO_4)_2$ system, theoretical calculations involving electrostatic potential distribution, band alignment, and photogenerated carrier migration were performed [58]. Based on the energy-level parameters shown in Fig. 8a and b, the work functions of CdS NPs and $AgIn(WO_4)_2$ were calculated to be 4.94 and 5.61 eV, respectively, revealing a pronounced Fermi-level difference between the two semiconductor components. Due to the larger work function and lower Fermi level of $AgIn(WO_4)_2$, electrons spontaneously migrate from CdS NPs toward $AgIn(WO_4)_2$ upon intimate interfacial contact, inducing interfacial charge redistribution and establishing a favorable charge-transfer pathway within the ternary heterostructure. Band alignment analysis (Fig. 8c) further demonstrates that the CdS/Pt/$AgIn(WO_4)_2$ system exhibits a typical type-II band alignment, in which Pt NPs function as electron-transfer mediators to accelerate directional electron migration and facilitate the spatial separation of photogenerated carriers. Accordingly, the proposed photogenerated-carrier migration pathway in the CdS/Pt/$AgIn(WO_4)_2$ system is illustrated in Fig. 8d.

Under photoirradiation, electron-hole pairs are generated in both semiconductors. The electrons in the conduction band (CB) of CdS NPs migrate toward the CB of $AgIn(WO_4)_2$ through the Pt NPs cocatalyst, participating in H^+ reduction, while the photogenerated holes are rapidly consumed by the lactic acid sacrificial agent. This type-II heterojunction configuration enables efficient directional carrier migration and spatial charge separation, thereby suppressing electron-hole recombination and enhancing photocatalytic hydrogen evolution performance. Further electronic structure analysis (Fig. 8e) reveals distinct electron accumulation and depletion regions at the CdS/Pt/$AgIn(WO_4)_2$ interface, confirming the role of Pt NPs as electron-transfer mediators and active sites that accelerate interfacial charge migration. Based on the calculated results, the transferred electron quantity reaches approximately 3.89 e, providing direct evidence of strong electronic coupling among CdS NPs, Pt NPs, and $AgIn(WO_4)_2$, which effectively promotes the separation of photogenerated electron-hole pairs.

In addition, Fig. S14 illustrates the charge-density difference profile of the CdS/Pt/$AgIn(WO_4)_2$ system along the z-axis. The profile demonstrates pronounced charge-density variations at the interface, where positive and negative values represent electron accumulation and depletion regions, respectively. These distinct charge redistribution features are mainly concentrated at the interfaces among CdS NPs, Pt NPs, and $AgIn(WO_4)_2$, confirming substantial interfacial electron rearrangement, which is essential for facilitating directional charge transfer.

4. Conclusion

Herein, a CdS/Pt/$AgIn(WO_4)_2$ ternary composite photocatalyst was successfully constructed by employing tubular $AgIn(WO_4)_2$ as the supporting matrix through the integration of hydrothermal treatment and in situ photoreduction deposition. The introduction of CdS NPs enhances visible-light harvesting, while the interfacially distributed Pt NPs promote directional electron transfer from CdS NPs to $AgIn(WO_4)_2$. The optimized CdS/Pt/$AgIn(WO_4)_2$ sample exhibits outstanding photocatalytic hydrogen evolution performance, achieving a hydrogen evolution rate of 6.54 $mmol \cdot g^{-1} \cdot h^{-1}$, which is approximately 30 and 5 times higher than those of pristine $AgIn(WO_4)_2$ nanotubes and CdS NPs, respectively. Comprehensive experimental characterizations combined with theoretical calculations reveal the enhanced photocatalytic pathway within the ternary system. Strong interfacial coupling among the three components establishes an efficient charge-transfer network, in which Pt NPs act as critical electron-conducting bridges to facilitate directional electron migration and charge separation while suppressing electron-hole recombination. Furthermore, the active sites of Pt NPs exhibit a Gibbs free energy of hydrogen adsorption (ΔG_H^*) close to the thermoneutral value, enabling favorable H* adsorption and reducing the thermodynamic barrier for hydrogen evolution. The synergistic contributions of structural coupling, charge-transfer regulation, and accelerated surface reaction kinetics collectively account for the enhanced photocatalytic performance of the CdS/Pt/$AgIn(WO_4)_2$ composite. This work provides an effective design strategy for developing efficient and durable CdS-based multicomponent photocatalysts for solar-driven hydrogen production.

CRediT authorship contribution statement

Quanmei Zhou: Writing – original draft, Validation, Investigation. **Jiayi Meng:** Methodology. **Yifan Liao:** Formal analysis. **Yuchen Wei:** Investigation. **Bite Deng:** Writing – review & editing. **Yuying Hu:** Validation. **Hongyan Zhao:** Formal analysis. **Yakun Song:** Data curation. **Mohan Zhang:** Formal analysis. **Wei-Lin Dai:** Writing – review & editing, Visualization, Supervision, Project administration.

Declaration of competing interest

The authors declare that they have no known competing financial interests or personal relationships that could have appeared to influence the work reported in this paper.

Acknowledgements

This work was funded by the National Key Research and Development Program of China (2021YFA1501404), and the Science and Technology Commission of Shanghai Municipality (2024ZDSYS02).

Appendix A. Supplementary data

Supplementary data to this article can be found online at https://doi.org/10.1016/j.cej.2026.181451.

Data availability

Data will be made available on request.

References

[1] M.-Y. Qi, M. Conte, M. Anpo, et al., Cooperative coupling of oxidative organic synthesis and hydrogen production over semiconductor-based photocatalysts, Chem. Rev. 121 (2021) 13051–13085.
[2] J. Zhang, K. Shen, C. Xu, et al., Dual-channeled organic-inorganic hybrid architecture: Leveraging a unique photosensitive semiconductor for enhanced photocatalytic hydrogen evolution, Appl. Catal. B 366 (2025) 125025.

[3] Z. Zou, J. Ye, K. Sayama, et al., Direct splitting of water under visible light irradiation with an oxide semiconductor photocatalyst, Nature 414 (2001) 625–627.
[4] X. Chen, S. Shen, L. Guo, et al., Semiconductor-based photocatalytic hydrogen generation, Chem. Rev. 110 (2010) 6503–6570.
[5] H. Wang, L. Zhang, Z. Chen, et al., Semiconductor heterojunction photocatalysts: Design, construction, and photocatalytic performances, Chem. Soc. Rev. 43 (2014) 5234–5244.
[6] C.J. Verhoef, R. Ma, J.C. Slootweg, Mechanistic insights into light-driven acceptorless dehydrogenation reactions, Chem. Rev. 126 (2026) 5316–5353.
[7] D. Czekanowska, H. Salazar, J. Sáiz, et al., Interfacially coupled Bi_2WO_6@WS_2-PVDF based film for sonophotocatalytic trimethoprim removal: From material engineering to surface- and groundwater applications, Chem. Eng. J. 537 (2026) 176180.
[8] X. Wang, C. Peng, Y. Xiao, et al., Surface engineering enhancing activity and stability of Bi_2WO_{6-X} for selective C-H bond photooxidation, Chin. J. Catal. 81 (2026) 246–258.
[9] B. Urupalli, D.-S. Kim, G.-S. Shin, et al., Strategic core-shell integration for advancing Z-scheme heterojunctions: Interface-engineered $ZnIn_2S_4$/Ag_2WO_4@Ag ternary architecture for enhanced visible-light-driven photocatalytic H_2 production and pollutant degradation, Small 21 (2025) 2501833.
[10] H. He, S. Xue, Z. Wu, et al., Sonochemical fabrication, characterization and enhanced photocatalytic performance of Ag_2S/Ag_2WO_4 composite microrods, Chin. J. Catal. 37 (2016) 1841–1850.
[11] C. Chen, H. Shi, X. Cai, et al., Enhanced bifunctional photocatalytic performances for H_2 evolution and HCHO elimination with an S-scheme $CoWO_4$/$CdIn_2S_4$ heterojunction, Acta Phys. Chim. Sin. 41 (2025) 100155.
[12] R.-X. Bi, Z.-H. Peng, L. Lei, et al., Enhanced photocatalytic U(VI) reduction via double internal electric field in $CoWO_4$/covalent organic frameworks p-n heterojunction, J. Hazard. Mater. 475 (2024) 134869.
[13] S. Song, Y. Zhang, Y. Xing, et al., Rectangular $AgIn(WO_4)_2$ nanotubes: A promising photoelectric material, Adv. Funct. Mater. 18 (2008) 2328–2334.
[14] M. Fan, A. Qian, X. Han, et al., One-dimensional CdS/TpPa-COF S-scheme heterojunctions enabling directional charge transport for highly efficient photocatalytic hydrogen evolution, Adv. Funct. Mater. 36 (2026) e75647.
[15] H. Zhang, H. Liu, Z. Yuan, et al., Atomic-scale vacancy engineering in $NiPS_3$/CdS S-scheme heterojunction for efficient photocatalytic hydrogen production, Appl. Catal. B 381 (2026) 125826.
[16] Y.-T. Liu, M.Y. Ma, X.-Z. Cheng, et al., Engineering electron lifetime for high-performance heterostructured 1D CdS photocatalyst, Small 21 (2025) 2412588.
[17] C. Yuan, W. Xia, J. Wang, et al., A dual-functional single-atom modified SnS_2/CdS S-scheme photocatalyst for synergistic hydrogen production and lactic acid oxidation: A DFT study, Acta Phys. -Chim. Sin. 42 (2026) 100244.
[18] H. Long, R. Li, C. Bie, et al., Self-disproportionation-induced H-adsorption/desorption zones in amorphous nickel boride cocatalyst for efficient photocatalytic hydrogen evolution, J. Am. Chem. Soc. 148 (2026) 17146–17156.
[19] B. Hu, M. Wu, X. Lv, et al., Interfacial electric fields from triboelectric-photocatalytic coupling drive efficient hydrogen evolution, Chem. Eng. J. 538 (2026) 176644.
[20] H. Wang, Y. Hao, T. Shu, et al., Controllable synthesis of large-scale $SnSe_2$ nanosheet arrays and Te/$SnSe_2$ vertical mixed-dimensional heterostructures for hydrogen evolution reaction, Appl. Phys. Lett. 127 (2025) 113902.
[21] S. Tang, W. Wang, L. Lei, et al., In situ photo-deposition of amorphous nickel boride nanocluster onto graphitic carbon nitride for significantly promoting light-driven hydrogen evolution, Int. J. Hydrogen Energy 148 (2025) 150076.
[22] L. Lei, Y. Fan, Y. Jia, et al., Salt-assisted activation of n → π^* electronic transition in orange carbon nitride for enhanced visible-light-driven H_2 generation, J. Mater. Chem. A 13 (2025) 2836–2848.
[23] Y. Zhao, X. Wu, H. Wang, et al., Phosphorus regulates coordination number and electronegativity of cobalt atomic sites triggering efficient photocatalytic water splitting, Nano Lett. 24 (2024) 16175–16183.
[24] Z. Liu, Y. Shan, L. Fan, et al., Partial disruption of coordination bonds triggers MOF amorphization for efficient electrocatalytic nitrate reduction to ammonia, Adv. Funct. Mater. 36 (2026) e76580.
[25] J.Y. Do, R.K. Chava, Y.I. Kim, et al., Fabrication of Ag based ternary nanocomposite system for visible-light photocatalytic hydrogen evolution reaction, Appl. Surf. Sci. 494 (2019) 886–894.
[26] Y. Zhou, K. Gao, Y. Song, et al., Binary direct vs. ternary electron-mediated Z-scheme heterojunctions: Unraveling pathway-engineered carrier dynamics for photocatalytic hydrogen evolution, Appl. Catal. B 382 (2026) 126002.
[27] J.J. Delgado, E. Bu, Y. Han, et al., From single atoms to nanoparticles: pathways toward efficient and durable Pt/TiO_2 photocatalysts, Adv. Funct. Mater. 36 (2026) e22917.
[28] H. Li, H. Jiao, X. Zhang, et al., Functional groups induced microenvironment regulation of Pt catalytic sites in MOF/COF heterojunction for enhanced photocatalytic hydrogen evolution, Adv. Funct. Mater. 36 (2026) e75908.
[29] N. Tian, C. Yuan, T. Zhou, et al., Defect-coordinated Au nanoparticles in carbon nitride for efficient piezo-photocatalytic hydrogen peroxide production, Chin. J. Catal. 81 (2026) 272–283.
[30] X. Fan, C. Zhang, M. Chen, et al., Single-particle catalytic monitoring of interfacial charge dynamics during light-driven CdS shell growth on Au nanocubes, Nat. Commun. 17 (2026) 5988.
[31] W. Zhan, N. Yang, T. Zhou, et al., Construction of Ag single atoms and nanoparticles co-modified g-C_3N_4 for synergistic plasma photocatalytic broad-spectrum hydrogen production, Chin. J. Catal. 79 (2025) 162–173.
[32] W. Zhang, D. Jiao, H. Liu, et al., Atomic-site synergy in Ag-Co dual-metal-site photocatalyst steering highly selective NO-to-nitrate conversion with inhibiting NO_2 emission, Appl. Catal. B 384 (2026) 126145.
[33] H. Zhang, H. Gu, X. Wang, et al., Fabrication of noble-metal-free hierarchical rectangular tubular S-scheme NiS/$ZnIn_2S_4$/$AgIn(WO_4)_2$ nanocomposite for highly efficient photocatalytic hydrogen evolution, Chem. Eng. J. 457 (2023) 141185.
[34] J. Meng, J. Zhang, Y. Huang, et al., Superior bridging effect of Pt NPs in all-solid-state Z-scheme CdS QDs/$NaTaO_3$ microcube heterojunction for highly efficient photocatalytic hydrogen evolution, Chem. Eng. J. 525 (2025) 170413.
[35] H. Huang, Y. Cai, Q. Xu, et al., S-scheme CdS/Co_3S_4 double-shelled hollow nanoboxes for enhanced photocatalytic hydrogen evolution, Small 21 (2025) 2501710.
[36] K. Zhao, M. Luo, Y. Zhang, et al., Coupled cation-electron transfer at the Pt(111)/perfluoro-sulfonic acid ionomer interface and its impact on the oxygen reduction reaction kinetics, Nat. Catal. 8 (2025) 46–57.
[37] Z.-F. Cai, M.A. Manae, Z.-X. Tang, et al., Mechanistic insights into nitroarene hydrogenation dynamics on Pt(111) via in situ tip-enhanced Raman spectroscopy, J. Am. Chem. Soc. 147 (2025) 39838–39845.
[38] Y. Wu, P.T.T. Nguyen, S.S. Wong, et al., Photocatalytic upcycling of polylactic acid to alanine by sulfur vacancy-rich cadmium sulfide, Nat. Commun. 16 (2025) 846.
[39] C. Cheng, J. Zhang, B. Zhu, et al., Verifying the charge-transfer mechanism in S-scheme heterojunctions using femtosecond transient absorption spectroscopy, Angew. Chem. Int. Ed. 62 (2023) e202218688.
[40] T. Guo, G. Hu, J. Liu, et al., Defect-enhanced charge separation in ZnCdS/WS_2 S-scheme heterojunctions: engineering sulfur vacancies to facilitate photocatalytic H_2 production, Chin. J. Struct. Chem. 45 (2026) 100960.
[41] P. Ding, Z. Fu, L. Zhang, et al., Synergistic effect of charge-transfer bridge and surface defects for highly efficient photothermal catalytic CO_2 reduction over 2D/3D $SrTiO_3$/$Zn_{0.5}Cd_{0.5}S$, Chem. Eng. J. 515 (2025) 163637.
[42] Q. Liang, J. Fan, X. Deng, et al., Oxygen vacancy-driven asymmetrical charge distribution on Bi-O-Sn sites in Sn-doped Bi_2MoO_6 for efficient photocatalytic CO_2-to-CH_4 conversion, Angew. Chem. Int. Ed. 65 (2026) e21874.
[43] Y. Xie, M. Li, F. Tong, et al., Synergy of atom doping and vacancy engineering in $ZnIn_2S_4$ for enhanced photocatalytic plastic reforming coupled with H_2 evolution, Appl. Catal. B 388 (2026) 126548.
[44] M.-Y. Liu, J.-Y. Tang, H.-W. Zhu, et al., High-density twin-crystal CdS enhances photocatalytic CO_2 reduction by efficient electron utilization, Adv. Funct. Mater. 36 (2026) e75344.
[45] J. Liu, Z. Liu, P. Lu, et al., Lewis acid-base dual sites enabled by Mg^{2+} doping in CdS quantum dots for selective photocatalytic CO_2 reduction to CH_4, Adv. Funct. Mater. 36 (2026) e09666.
[46] X. Wang, L. Han, X. Li, et al., Z-scheme heterojunction in CdS-decorated 3D flower-like $CdIn_2S_4$ nanospheres for enhancing visible light-driven CO_2 reduction, Nano Res. 18 (2025) 94908239.
[47] Z. Xia, L. Lin, X. Chen, et al., Solar-driven upcycling of polylactic acid to alanine over Pt/CdS-TiO_2 heterojunction single-atom photocatalyst, J. Am. Chem. Soc. 147 (2025) 45357–45365.
[48] Z. Meng, J. Zhang, H. Long, et al., Kelvin probe force microscopy reveals spatially resolved charge-transfer mechanism in CdS/BiOBr S-scheme heterojunction photocatalyst, Angew. Chem. Int. Ed. 64 (2025) e202505456.
[49] F. Liu, X. Li, B. Sun, et al., Building hollow multi-shell structured Zn_2MnO_4/CdS S-scheme heterojunction for boosted photocatalytic H_2 production, J. Mater. Sci. Technol. 250 (2026) 233–242.
[50] J. Meng, Y. Huang, Y. Liao, et al., Ag-doping modulates the built-in electric field in S-scheme heterojunction of $ZnIn_2S_4$/covalent organic framework for efficient photocatalytic hydrogen peroxide production from pure water, J. Colloid Interface Sci. 700 (2025) 138603.
[51] X. Wang, H. Zhang, Y. Huang, et al., Nitrogen defects and interfacial chemical bonds in Fe single-site mediated C_3N_4 with rod-like Fe_2O_3 enhanced the S-scheme heterojunction for efficient energy conversion, Adv. Funct. Mater. (2025) 2421847.
[52] H. Zhang, Y. Huang, X. Wang, et al., Tightly-bound interfaces between $ZnIn_2S_4$ nanosheets and few-layered Mo_2TiC_2 MXene induced highly efficient noble-metal-free Schottky junction for photocatalytic hydrogen evolution, Sep. Purif. Technol. 360 (2025) 131199.
[53] Y. Zhang, Y. Huang, X. Wang, et al., Interface interaction modulates charge transfer in flower-like In_2S_3 nanosheets/COF composite for efficient solar-to-H_2O_2 conversion, Sep. Purif. Technol. 358 (2025) 130374.
[54] Y. Li, Y. Huang, H. Zhang, et al., In-situ construction of 3D/2D $ZnIn_2S_4$/Ni-MOLs: Highly efficient visible-light-driven photocatalytic heterojunction in hydrogen evolution, Appl. Catal. B 361 (2025) 124657.
[55] X. Wang, Y. Huang, H. Zhang, et al., Uniform nanorhombic A-Fe_2O_3 on g-C_3N_4 nanosheet: 2D/2D lattice matched S-scheme heterojunction towards efficient styrene oxidation and H_2 evolution, J. Catal. 439 (2024) 115746.
[56] A.D. Becke, Density-functional exchange-energy approximation with correct asymptotic behavior, Phys. Rev. A 38 (1988) 3098–3100.
[57] J.P. Perdew, K. Burke, M. Ernzerhof, Generalized gradient approximation made simple, Phys. Rev. Lett. 77 (1996) 3865–3868.
[58] S.J. Clark, M.D. Segall, C.J. Pickard, et al., First principles methods using CASTEP, Z. Kristallogr. Cryst. Mater. 220 (2005) 567–570.